



Visualisation of Electromagnetic Fields by Use of a Numerical Method

William Bulmer

Supervisor: Professor D. P. Hampshire

Department of Physics

Durham University

April 26, 2023

Abstract

The mathematical formulae used in the popular FDTD method have been derived in three dimensions for a point source. Use of these to undergo computational simulations by way of iterative processes is studied, and the limitations of the method are considered. A well known revision to the theory has been used to provide numerical boundary conditions, which prevent reflections entering the problem space. The algorithm has been rigorously verified through analysis of power, double-slit diffraction and an infinitesimal dipole, all yielding results in accordance with established solutions. Analysis of an AC current carrying transparent wire-loop was performed which produced results that matched the analytical solution of a Hertzian dipole. Additional analysis of a AC current carrying conducting wire-loop was conducted, with results comparable to that of the transparent wire.

Contents

1	Introduction	1
2	The Finite-Difference Time-Domain Method	2
2.1	The Yee-Grid	2
2.2	The Update Equations	2
2.3	Numerical Limitations	3
2.4	The Perfectly Matched Layer - PML	4
3	Development of the FDTD simulation	6
3.1	Hard and Soft Sources	6
3.2	One-Dimensional Simulation	6
3.3	Two-Dimensional Simulation	7
4	Validity of the FDTD Simulation	8
4.1	Spherical Symmetry of a 3D Simulation	8
4.2	Power Analysis	11
4.3	Infinitesimal Dipole	12
4.4	Reproduction of the Double Slit Experiment	14
5	Analysis of a Magnetic Dipole	15
5.1	Construction of The Wire Loop	15
5.2	Transparent Wire Loop Results	17
5.3	Conductive Wire Loop Results	19
6	Discussion	23
6.1	Choosing FDTD	23
6.2	Code Development	23
6.3	Future Improvements	23
7	Conclusion	24
8	Acknowledgements	25
9	References	26
10	Appendix	27
10.1	Three Dimensional Update Equations	27

1. Introduction

Electrodynamics explores the interactions of moving electric charges with varying electric and magnetic fields, an important phenomena that has many useful scientific and technological applications. Using the previous works of Faraday, Ampère, Gauss and Coulomb; James C. Maxwell formulated a system of four equations that summarises the classical theory of electrodynamics. In vector form, these are:

$$\nabla \cdot \underline{E} = \frac{\rho}{\epsilon_0} \quad (1.1)$$

$$\nabla \cdot \underline{B} = 0 \quad (1.2)$$

$$\nabla \times \underline{E} = -\frac{\partial \underline{B}}{\partial t} \quad (1.3)$$

$$\nabla \times \underline{B} = \mu_0 \underline{J} + \mu_0 \epsilon_0 \frac{\partial \underline{E}}{\partial t} \quad (1.4)$$

Where E is the electric field strength, ρ is the electric charge density, B is the magnetic flux density and J is the current density. The equations can be supplemented by Ohm's law (1.5) and the constitutive relations, which governs how electromagnetic waves propagate through dielectrics (1.6) and magnetised materials (1.7):

$$\underline{J} = \sigma_n \underline{E} \quad (1.5)$$

$$\underline{D} = \epsilon_0 \epsilon_r \underline{E} \quad (1.6)$$

$$\underline{B} = \mu_0 \mu_r \underline{H} \quad (1.7)$$

Where σ_n is the electrical conductivity; μ_r and ϵ_r are relative properties of the respective materials; D and H are the auxiliary fields.

For multidimensional systems of complex geometries, Maxwell's equations can become impossible to find exact solutions for, and we must rely on crude approximations that deviate from reality. Numerical methods allow an approximate solution to be found, limited only by the computing processing power on hand. A popular approach to be discussed in detail, is the finite-difference time-domain method (FDTD). The technique models continuous space as discrete points on a 3D grid, each with a field value associated with it. By use of the central difference approximation in first order (1.8), a leap frog algorithm can be created by using two adjacent E fields to determine the corresponding adjacent B field (and vice versa).

$$\frac{\partial f(x)}{\partial x} = \frac{f\left(x + \frac{\Delta_x}{2}\right) - f\left(x - \frac{\Delta_x}{2}\right)}{\Delta_x} \quad (1.8)$$

The well known mathematical formulation used in the algorithm will be derived while

investigating its limitations. Insight and derivation of the necessary numerical boundary conditions will also be explored.

2. The Finite-Difference Time-Domain Method

2.1. The Yee-Grid

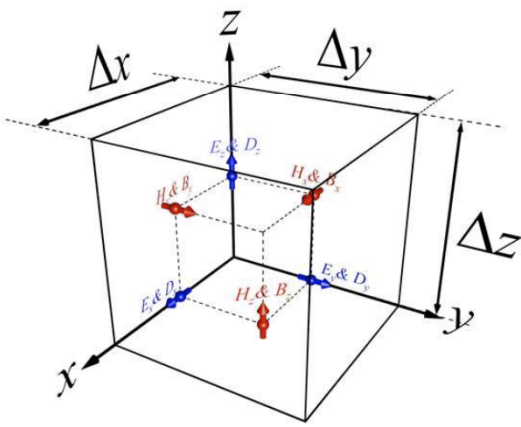


Figure 1: Yee-Grid: Staggered spatial grid used in FDTD for solving Maxwell's equations. Electric fields are to exist at full space and time steps, while magnetic fields are to exist at half space and time steps [8]. These are the unit cells in the computational domain which are iterated over. An exploded view of the deltas shows the length of each side on the Yee-grid

A major advantage of staggering the fields as shown in Figure 1 is that Maxwell's first (for $\rho=0$), (1.1) and second equations (1.2) are automatically satisfied, resulting in only (1.3) and (1.4) needing to be considered. A consequence of the Yee-Grid that must be considered is that fields components in the same unit cell are out of phase, and so this must be accounted for upon source injections.

2.2. The Update Equations

The mathematical formulae which enables the leap frog algorithm are referred to as the 'update equations'. We begin by rewriting Maxwell's equations (1.3 - 1.4) in differential form. For a streamlined focus on the algorithm's primary technique, we simplify the problem by first modelling a point source in a vacuum. This allows omission of the constitutive relations (1.5 - 1.7), which may be implemented via a modular process for more complex problems.

$$\begin{aligned} \left[\left(\frac{\partial E_z}{\partial y} - \frac{\partial E_y}{\partial z} \right), \left(\frac{\partial E_x}{\partial z} - \frac{\partial E_z}{\partial x} \right), \left(\frac{\partial E_y}{\partial x} - \frac{\partial E_x}{\partial y} \right) \right] &= - \frac{\partial B}{\partial t} \\ \left[\left(\frac{\partial B_z}{\partial y} - \frac{\partial B_y}{\partial z} \right), \left(\frac{\partial B_x}{\partial z} - \frac{\partial B_z}{\partial x} \right), \left(\frac{\partial B_y}{\partial x} - \frac{\partial B_x}{\partial y} \right) \right] &= \mu_0 \epsilon_0 \frac{\partial E}{\partial t} \end{aligned} \quad (2.1)$$

For further simplicity, we choose to collapse the problem into one dimension without loss of

generality. Maxwell's equations then become two independent modes. Selecting the arbitrary axis z ($\partial/\partial x = \partial/\partial y = 0$) and using the central difference approximation (1.8) for space and time (E_x/B_y mode), we have:

$$\begin{aligned}\frac{E_x(z + \Delta z, t) - E_x(z, t)}{\Delta z} &= \left[\frac{B_y(z, t + \frac{\Delta t}{2}) - B_y(z, t - \frac{\Delta t}{2})}{\Delta t} \right] \\ \frac{B_y(z, t + \frac{\Delta t}{2}) - B_y(z - \Delta z, t + \frac{\Delta t}{2})}{\Delta z} &= \mu_0 \epsilon_0 \left[\frac{E_x(z, t + \Delta t) - E_x(z, t)}{\Delta t} \right]\end{aligned}\quad (2.2)$$

It is ensured that while the electric and magnetic fields are staggered by half-grid steps on the Yee-Grid, the electric and magnetic field's yielded from our approximations agree on the same positions in space and time. Converting these into index form and rearranging, we achieve the result:

$$\begin{aligned}B_y|_{k+\frac{1}{2}}^{n+\frac{1}{2}} &= B_y|_{k+\frac{1}{2}}^{n-\frac{1}{2}} + \Delta t \frac{E_x|_{k+1}^n - E_x|_k^n}{\Delta z} \\ E_x|_k^{n+1} &= E_x|_k^n + \frac{\Delta t}{\mu_0 \epsilon_0} \frac{B_y|_{k+\frac{1}{2}}^{n+\frac{1}{2}} - B_y|_{k-\frac{1}{2}}^{n+\frac{1}{2}}}{\Delta z}\end{aligned}\quad (2.3)$$

Where the index k is analogous to a Yee-Grid point along the z axis, and index n is analogous to a time step. Using the above result (2.3), a field at a later time step can be calculated using fields at previous time steps. It is this mechanism that allows the 'leapfrogging' algorithm to occur, and so this concludes the derivation. Every iteration of the algorithm will move forward at a pace of $\Delta t / 2$ and we will discover in the next section that in order to ensure algorithm stability, Δt must satisfy a certain condition.

2.3. Numerical Limitations

A vulnerability of FDTD, like all iterative algorithms, is the possibility of diverging solutions. In order to prevent this, we deploy the Courant-Friedrichs-Lowy stability condition[9] in three dimensions:

$$\Delta t < \frac{1}{c \sqrt{\frac{1}{\Delta x^2} + \frac{1}{\Delta y^2} + \frac{1}{\Delta z^2}}}\quad (2.4)$$

This ensures that a physical wave would not propagate farther than a single unit cell in one time step, and so information from a given field can only propagate to its immediate neighbour. This value (2.4) must also be multiplied by the smallest refractive index on our grid if we were to incorporate materials.

Additionally, numerical dispersion must also be considered. In continuous medium we expect a constant phase velocity for a given frequency but in discretized space, this phase velocity becomes dependent on the direction of propagation and grid resolution. The error is enhanced for larger grid spacing, sources of higher frequency and angles of propagation

non-parallel with the grid axes. A first attempt at minimisation was to select a condition on the length of our unit cells. A sensible choice used was :

$$\Delta x = \frac{\lambda_{min}}{20} \quad (2.5)$$

where λ_{min} is the minimum discernible wavelength which we wish to study. Finally, in order to maintain a high level of accuracy, the electric field quantities must be scaled by the impedance so that the magnetic and electric fields are both of the same order of magnitude.

2.4. The Perfectly Matched Layer - PML

Observing the update equations derived in section 2 (2.3), we might question what happens at the boundaries of our problem space. The future electric field is determined by manipulation of a magnetic field positioned at a previous index. At the zeroth index, the electric field is unable to update, as the magnetic field needed has a negative index, and so does not exist in our problem space. Likewise, the magnetic field at the maximum index cannot be updated. By default, all fields are initialised to zero at the beginning of the program. This condition is equivalent to placing a perfect conductor at the boundaries of our grid which results in maximum reflection of a source wave back into our problem space. It is important that these reflections are eliminated so that we can make useful conclusions from our simulation without excessive 'traffic'. The most popular technique is to implement a PML.

Reflections are caused by a change in impedance, so it becomes necessary to 'perfectly match' the impedance through the fictitious material for all polarisation's, while introducing loss via an imaginary term.

$$\tilde{\epsilon}_r = \epsilon_r + \frac{\sigma}{j\omega} \quad (2.6)$$

The impedance is matched through the first term, while the loss is introduced via the second term. $\tilde{\epsilon}_r, \epsilon_r, \sigma$ are tensors that cover our problem space. They can be diagonalized via a change in coordinate system. One way to match the impedance to air (vacuum), is to have $\mu_r = \epsilon_r$ as follows.

$$[\mu_r] = [\epsilon_r] = \begin{bmatrix} a & 0 & 0 \\ 0 & b & 0 \\ 0 & 0 & c \end{bmatrix} \quad (2.7)$$

Snell's law determines the angle of transmission, while Fresnel's Laws are used to predict reflection and transmission which is dependent on the polarisation. Solving these equations for our ansatz (2.7) yields $a = b = \frac{1}{c}$ for waves crossing an interface perpendicular to the z-axis. Cyclic permutation of the reciprocal in addition to a renaming of the dummy variables

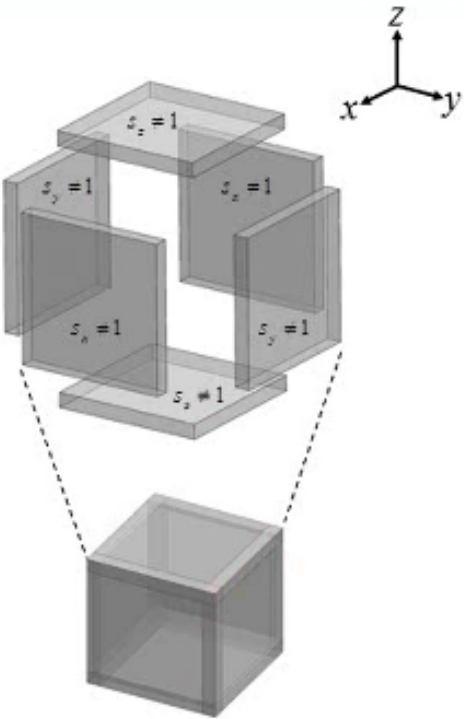


Figure 2: Pictured is an expanded view of the 'PML'. It consists of surrounding our problem space (computational space omitting PML), with a fictitious lossy medium to attenuate the incoming waves while simultaneously preventing reflections. The S components are the coefficients from which Maxwell's equations are multiplied. They are equal to 1 within our problem space. [8]

gives the full solution for waves crossing interfaces in three dimensions:

$$S = [S_x] \cdot [S_y] \cdot [S_z] = \begin{bmatrix} \frac{S_y S_z}{S_x} & 0 & 0 \\ 0 & \frac{S_x S_z}{S_y} & 0 \\ 0 & 0 & \frac{S_x S_y}{S_z} \end{bmatrix} \quad (2.8)$$

The PML loss terms used in this report have values given by:

$$\begin{aligned} S_x(x) &= 1 + \frac{\sigma_{x'}(x)}{j\omega\epsilon_0} \\ \sigma_{x'}(x) &= \frac{\epsilon_0}{2\Delta t} \left(\frac{x}{L_x} \right)^3 \end{aligned} \quad (2.9)$$

where x is the distance into our problem space from the boundary and L_x is the length of the PML. We can now incorporate the PML into Maxwell's equations in the frequency domain as follows:

$$\begin{aligned} \nabla \times \underline{E} &= -j\omega [S] \underline{B} \\ \nabla \times \underline{B} &= \mu_0 \epsilon_0 j\omega [S] \underline{B} \end{aligned} \quad (2.10)$$

Converting from the frequency domain back to the time domain can be achieved through Fourier Transform's which yields a new set of update equations. It can be verified that the updates equations should be identical to those previously defined until the PML regions are reached.

3. Development of the FDTD simulation

3.1. Hard and Soft Sources

Source implementation in FDTD can be done a multiple ways, two of them being by hard and soft sources. A hard source imposes a fixed value of the field at a specific point in the simulation grid; any incoming waves are overwritten. Soft sources however, add to existing field values at specific points. For the purpose of this report, only soft sources will be used since hard sources can lead to discontinuities and unwanted reflections. Soft sources also preserve the shape of the input waveform more accurately.

3.2. One-Dimensional Simulation

The initial development of the finite-difference time-domain (FDTD) algorithm began by establishing a strong foundation in one-dimension. The decision was driven by its ease of debugging due to fast simulation run times. An excitation source was introduced and its potential for divergence was examined. Given that continuous injection of energy into the simulation could complicate the detection of divergence, a Gaussian pulse source was selected due to its limited duration nature. Additionally the source was chosen to be soft to further expose divergence. The equation for the source wave can be written as:

$$E_z(t) = \sin(\omega t * \Delta t) \exp\left(-\frac{(t - t_0)^2}{\tau^2}\right) \quad (3.1)$$

where ω is the angular frequency of the source, t is our time step, Δt is the time-step size in seconds, τ is our pulse width, t_0 is time at which the pulse is peaked.

The Courant-Friedrichs-Lowy condition is satisfied with $\Delta t = \Delta x / c$, and so stable solutions are produced. The Dirichlet boundary conditions are a numerical artifact resulting from the inability of fields to update at the boundaries, due to the update equations requiring field values outside the simulation space. Waves propagating back into the simulation make analysis of more complex systems ineffective. For a one-dimensional simulation, a simple solution is to implement Mur absorbing boundary conditions:

$$E_z|_0^{t+1} = E_z|_1^t \quad (3.2)$$

$$B_y|_{200}^{t+1} = B_y|_{199}^t \quad (3.3)$$

By equating the edge value with the adjacent value from a previous time step, we approximate the wave to be propagating to infinity, eliminating reflections. This technique assumes incoming waves are parallel and so the method breaks down for higher dimensions, requiring a more sophisticated method such as the PML.

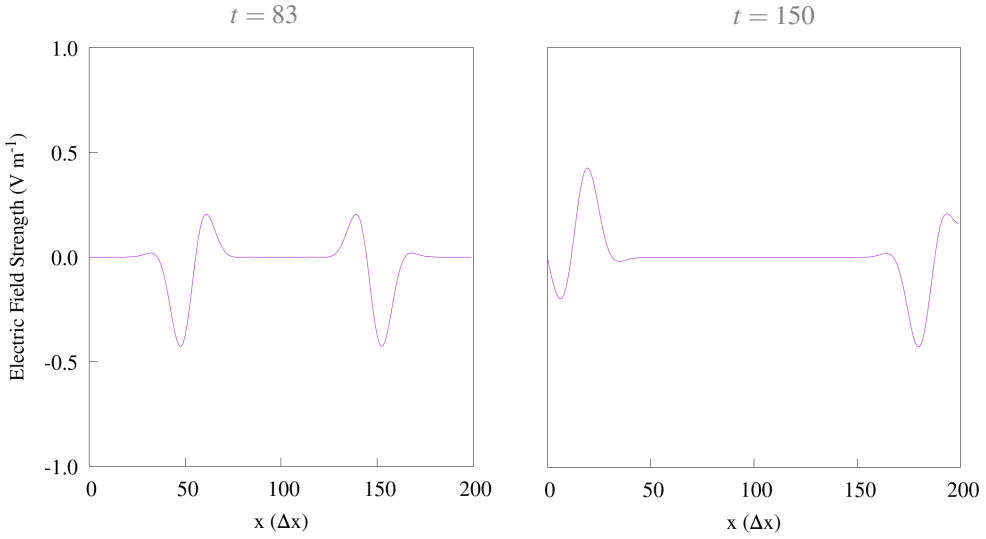


Figure 3: One-Dimensional FDTD simulation with Dirichlet boundary conditions. A soft Gaussian E_z point source is injected at $x = 100$, $t = 0$ and propagates along the x -axis. The two panels capture the same simulation at different time steps. The left panel shows the source propagating out from the center, while the right panel shows the source at a later time step propagating inward after reflection. Simulation parameters: $\tau = 12\Delta x$, $t_0 = 36\Delta x$, $\Delta x = 25nm$, $\omega = 1.88 \times 10^{15}s^{-1}$, and $\Delta t = 8.3 \times 10^{-17}s$

3.3. Two-Dimensional Simulation

Moving closer to achieving three-dimensional solutions while maintaining low computational time, the two-dimensional scenario was examined. From this point, it must be noted that the Yee-grid deployed has equal spacial resolutions in all three Cartesian directions. The same Gaussian pulse source used in the one-dimensional solution was again used. This was a good opportunity to introduce the PML while still maintaining ease of debugging. It was found that a length of $8\Delta x$ was large enough to ensure smooth transition of incoming waves into the PML, reducing potential reflections.

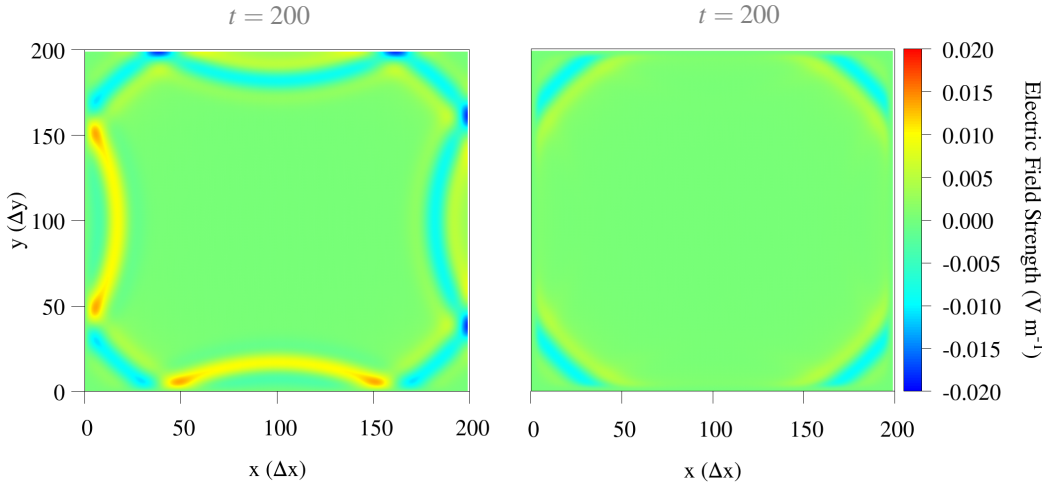


Figure 4: Two-Dimensional FDTD simulation of a Gaussian point source in a vacuum, injected at $x = 100$, $y = 100$, $t = 0$. Data points have been interpolated. Both panels are capturing a simulation at a time step of 200. The left panel has Dirichlet boundary conditions resulting in reflections. The right panel has a PML enclosing the simulation, which has thickness $8\Delta x$. Simulation parameters: $\tau = 12\Delta x$, $t_0 = 36\Delta x$, $\Delta x = 25\text{nm}$, $\omega = 1.88 \times 10^{15}\text{s}^{-1}$, and $\Delta t = 8.3 \times 10^{-17}\text{s}$

4. Validity of the FDTD Simulation

After achieving non-divergent propagation of electromagnetic waves, assessing the validity of the scheme against known analytical solutions was important. This section aims to give the reader confidence in the FDTD scheme developed.

4.1. Spherical Symmetry of a 3D Simulation

Many phenomena of interest exhibit spherical symmetry and so it is crucial to consider the potential deviations from this symmetry that may arise as an inherent property of a Cartesian-based scheme. It is anticipated that the simulation will exhibit deviations predominantly on the diagonals (non-parallel to the propagation axes). An attempt to minimise these was made by testing and adjusting specific grid parameters.

A preliminary definition of spherical coordinates is shown (Fig 3.) in order to avoid confusion.

The choice of source for this analysis was a soft sinusoidal point source (Fig 4.). The motivation for this was to test the algorithm's capability to handle time-dependent sources, which would not be possible with the Gaussian pulse source. One possible way to improve the spherical symmetry of the simulation would be to increase the spacial resolution. This enables higher resolution modelling of curved geometries and would also increase the accuracy of the field calculations. Due to RAM limitations, however, only improvements on the temporal

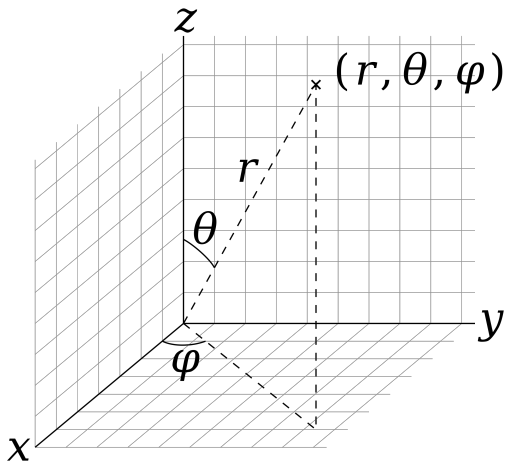


Figure 3: Spherical coordinates in three-dimensional space as defined by the ISO convention. The position of a point is specified by its distance from the origin (r), its azimuthal angle measured from the positive x -axis (φ), and its polar angle measured from the positive z -axis (θ).

resolution was examined. We modify the Courant-Friedrichs-Lowy stability condition by inclusion of the Courant number, r (Eq 4.1).

$$\Delta t < \frac{r}{c \sqrt{\frac{1}{\Delta x^2} + \frac{1}{\Delta y^2} + \frac{1}{\Delta z^2}}} \quad (4.1)$$

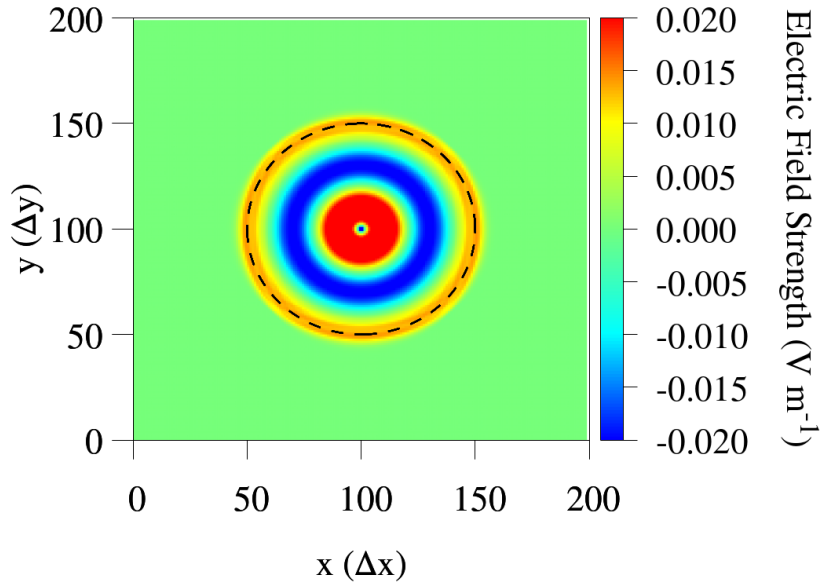


Figure 4: Two-dimensional FDTD simulation with a soft sinusoidal E_z point source injected at $x = 100$, $y = 100$. The plot is showing the field strength of E_z . Simulation parameters: $\Delta x = 25\text{nm}$, $\omega = 1.88 \times 10^{15}\text{s}^{-1}$, and $\Delta t = 8.3 \times 10^{-17}\text{s}$

Multiple simulations were run at constant parameters with exception to the Courant number, which was varied. Analysis of the spherical symmetry was performed at the same distance from the source; waves modelled with smaller Courant numbers take more time steps to propagate across the same unit grid, and so the simulation was run for longer time steps to account for this.

From figure 5, we observe that as we increase the temporal resolution, electric field values on the circumference of a given circle 'flatten' out as expected. The derivatives in Maxwell's equations are approximated by finite-differences in both space and time. Therefore, increasing the temporal resolution will result in better modelling of time-dependent behavior which includes oscillating electromagnetic waves.

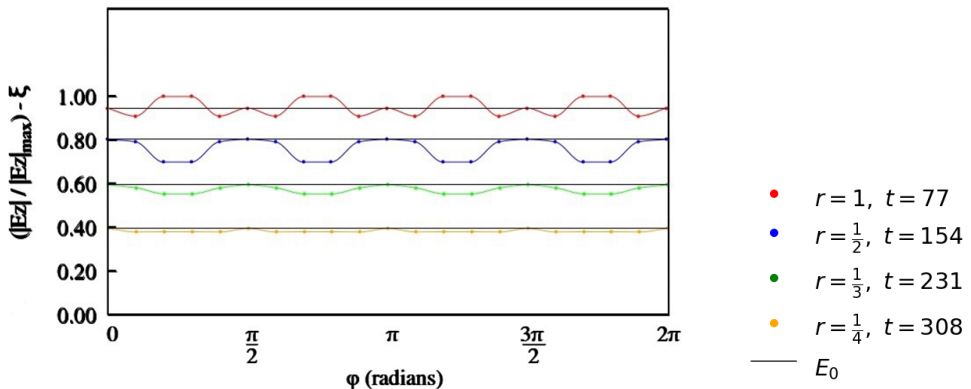


Figure 5: Angular dependence analysis of a 2D FDTD simulation in a vacuum: Figure shows a comparison of the normalized field values recorded at a radius of $50\Delta x$ from the source, for different Courant numbers and time steps. E_0 (black line) is the comparison value, which is the value of the E field at $\varphi = 0$ position, and values have been shifted by ξ (multiples of 0.2) for clarity.

4.2. Power Analysis

As a intermediate verification, a brief analysis of the power density was done. Energy propagating in a vacuum should experience no energy loss and the energy density should exhibit a decay of $1/r^2$ from the centre of the source. Performing the analysis in the xy-plane of a 2D simulation greatly simplifies the calculation of the Poynting vector (Eq 4.2).

$$\mathbf{S}_{xy} = \frac{1}{\mu_0} \begin{vmatrix} \hat{\mathbf{i}} & \hat{\mathbf{j}} & \hat{\mathbf{k}} \\ 0 & 0 & E_z \\ 0 & H_y & H_z \end{vmatrix} = \frac{1}{\mu_0} (E_z H_y) \hat{\mathbf{i}} - \frac{1}{\mu_0} (E_z H_z) \hat{\mathbf{j}} \quad (4.2)$$

where S_{xy} is the Poynting vector in the xy-plane where \mathbf{i} and \mathbf{j} components are the x and y components of the Poynting vector respectively.

Figure 6 shows a plot illustrating the magnitude and direction of the Poynting vector. After a large enough time such that the waves reach the boundary, We observe that for all positions on the grid, we see that the Poynting vector points radially outward from the centre, which aligns with expectation that energy propagation should be directed away from the source. The magnitude of the Poynting vector magnitude resembles a decay pattern which is in keeping with an intensity drop-off profile.

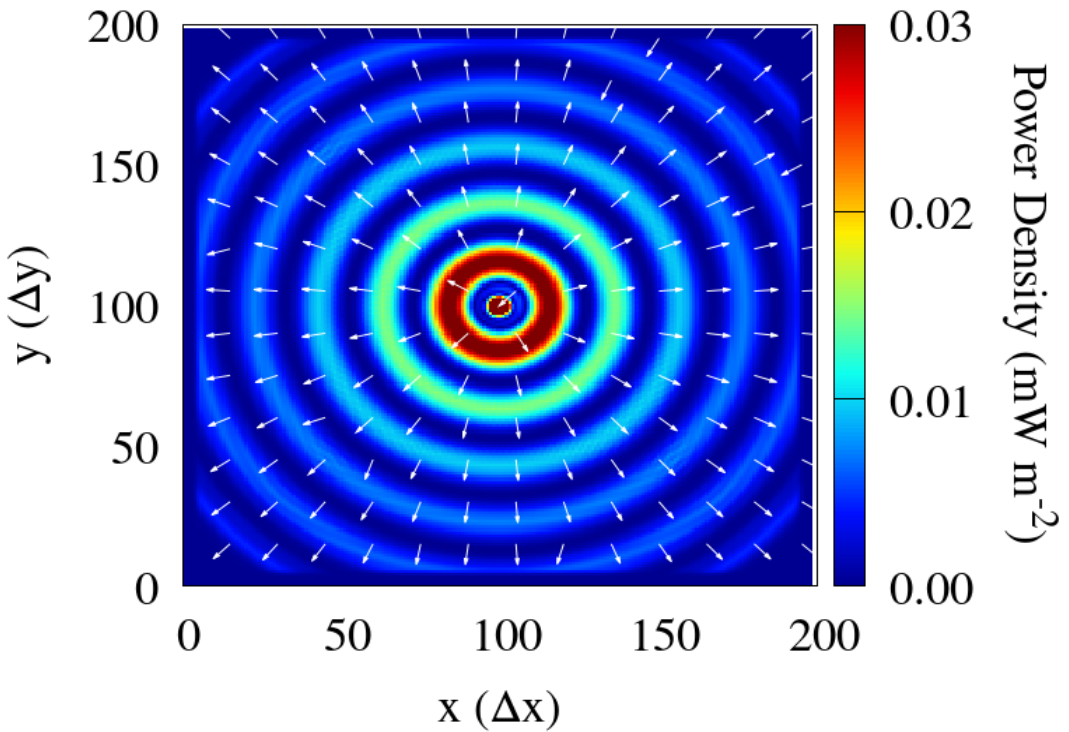


Figure 6: Magnitude of the Poynting vector for a sinusoidal E_z point source in a vacuum in two-dimensions. The arrows give the direction of the Poynting vector and thus, the direction of energy flow. Simulation parameters : $\Delta x = 25\text{nm}$, $\omega = 1.88 \times 10^{15}\text{s}^{-1}$, and $\Delta t = 2.1 \times 10^{-17}\text{s}$

4.3. Infinitesimal Dipole

After reducing numerical dispersion, a step closer to analysing the wire loop was to analyse an infinitesimal dipole in 3D. The same source from the angular dependence analysis was excited via E_x .

The analytic solution of Hertzian dipole[10] is given by (Eq 5) and so for an infinitesimal dipole, analysing the magnitude of the electric field in the xy-plane should present us with a modulated sine curve.

$$E_{\text{ff}} = \frac{\mu_0 I \Delta l}{4\pi r} \omega \sin \theta \sin(kr - \omega t) \hat{\theta} \quad (4.3)$$

It is important to note that this solution is only valid in the far-field. For an infinitesimal dipole, the length of the dipole is significantly smaller than the observation distance, and so we are indeed observing in the far-field. This is further supported by the residual plot (Figure 8).

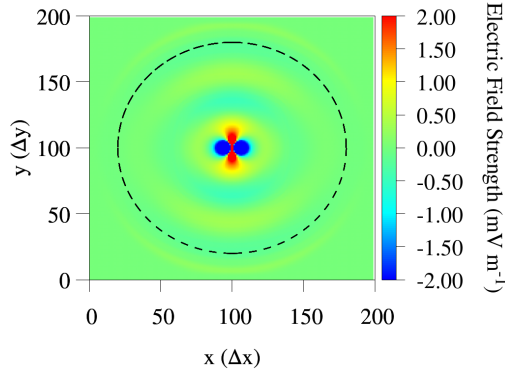


Figure 7: 3D-FDTD simulation of an infinitesimal dipole in a vacuum (E_x point source) as viewed from the xy-plane. Dashed line represents values to be taken for angular dependence analysis. Simulation parameters: Source $\lambda = 20\Delta x$, $\Delta x = 25$ nm, $\Delta t = 1.43\text{e-}18$ s $^{-1}$, $t = 677$

The simulated data for the infinitesimal dipole is in excellent agreement with the analytical data except the presence of a small magnitude of electric field in the $\varphi = 0$ direction. There should be no power flow/ propagation in the same as the orientation of a dipole. Possible causes for this may be due to numerical errors or due to the source implementation.

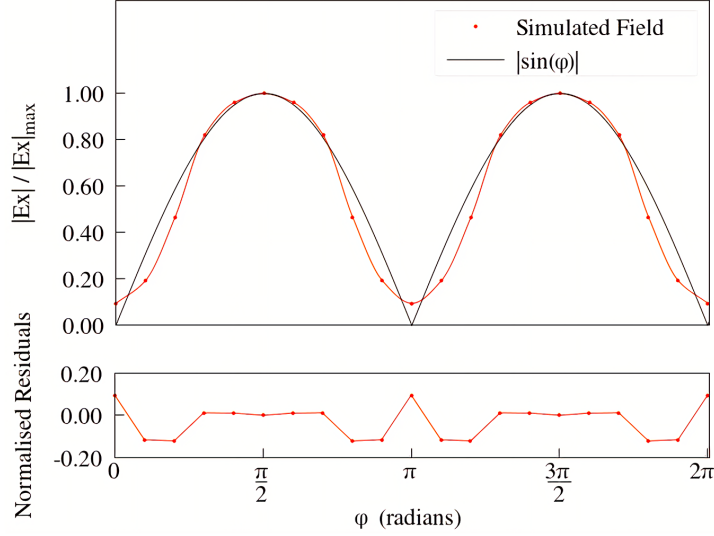


Figure 8: Angular dependence analysis of an infinitesimal dipole (E_x point source): The plot shows electric field values on a circle with radius = $50\Delta x$, normalised to the maximum intensity, as a function of the azimuthal angle φ . The dipole is viewed in the xy-plane with simulation parameters: Source $\lambda = 20\Delta x$, $\Delta x = 25$ nm, $\Delta t = 1.43 \times 10^{-18}$ s $^{-1}$, $t = 677$

4.4. Reproduction of the Double Slit Experiment

The objective of the report is the introduction of conductivity in a wire loop. This will present new solutions from that of a transparent wire loop, due to the introduction of reflection and diffraction. Therefore, it is important to assess the capability of the simulation at modelling diffraction. This was done by reproducing the famous double slit experiment. In order to compare simulated results to existing solutions, it was necessary to determine the regime our simulation was in, be it Fraunhofer or Fresnel.

$$L \gg \frac{d^2}{\lambda} \quad (4.4)$$

$$L \gg \frac{a^2}{\lambda} \quad (4.5)$$

$$I(\theta) \propto \frac{\left(\cos \frac{\pi a \sin \theta}{\lambda}\right)^2 \left(\sin \frac{\pi d \sin \theta}{\lambda}\right)^2}{\left(\sin \frac{\pi d \sin \theta}{\lambda}\right)^2} \quad (4.6)$$

where a is the slit width, d is the slit separation and L is the observation distance. For values of $a = 5\Delta x$, $d = 30\Delta x$ and $L = 130\Delta x$, we can perform simple calculations using (4.4)

and (4.5) to confirm that we are indeed in the Fraunhofer regime and so can approximate our intensity pattern[11] using the formula give in (4.6).

The same sinusoidal source used in angular dependence analysis was again used here. Any monochromatic source would also have worked.

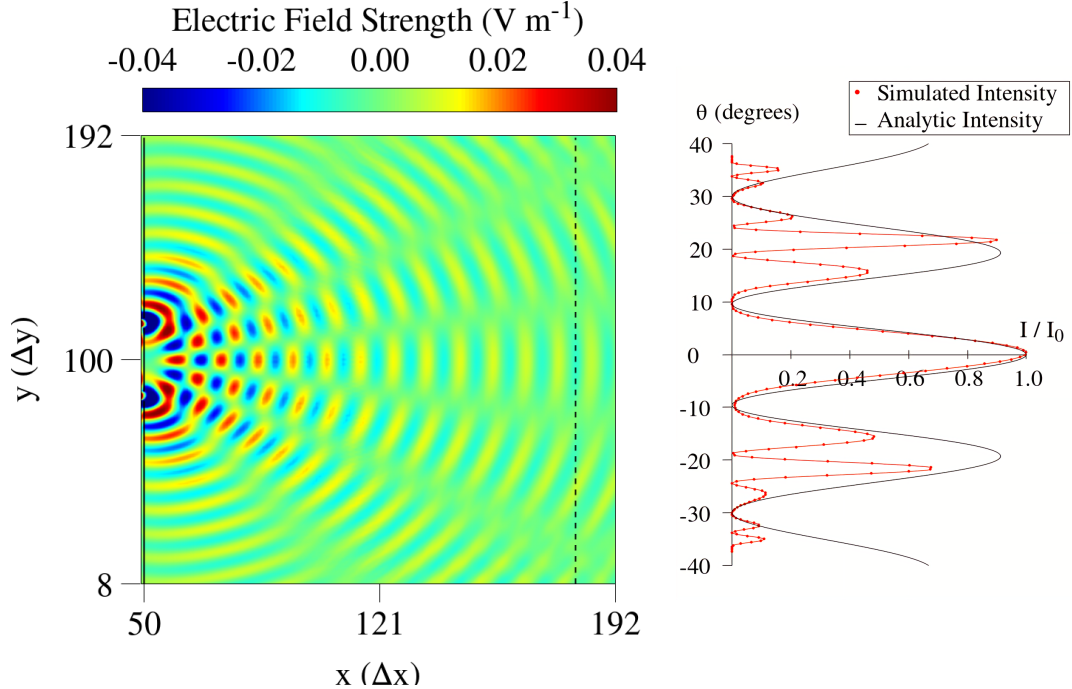


Figure 9: 3D-FDTD simulation of the double-slit experiment: On the left, an E_z point source placed at $x = 30$, $y = 100$ propagates through double slits centered on $x = 50$, $y = 100$. The right side shows the corresponding intensity pattern, calculated from E-field values at $x = 180$ (dashed line). The PML regions which are of length $8\Delta x$ are omitted. Simulation parameters: Source $\lambda = 10\Delta x$, slit width = $5\Delta x$, slit separation = $30\Delta x$, observation distance = $130\Delta x$, $\Delta x = 25$ nm, $\Delta t = 1.43\text{e-}18$ s $^{-1}$, $t = 1397$

The results obtained show excellent agreement with the predicted intensity confirming the simulation's ability to perform diffraction.

5. Analysis of a Magnetic Dipole

5.1. Construction of The Wire Loop

The introduction of current into the simulation was achieved by creating a transparent wire loop. The transparent wire loop acts only as a visual guide showing the placement of the current density; the material properties are equivalent to that of a vacuum. A convenient approach is to implement the current density as a soft source at each point within a toroidal structure which we use to model our wire (figure 10). The loop is completely defined by two parameters; a semi-major radius and a semi-minor radius. The spacial resolution is now

chosen such that we can model a realistic sized wire loop ($\Delta s = 1mm$), and the frequency is adjusted such that it oscillates to maximum value after 80 time steps ($w = 8.2 \times 10^{10} s$). Unfortunately, a uniform grid size of 200 unit cells was the upper limit due to memory limitations.

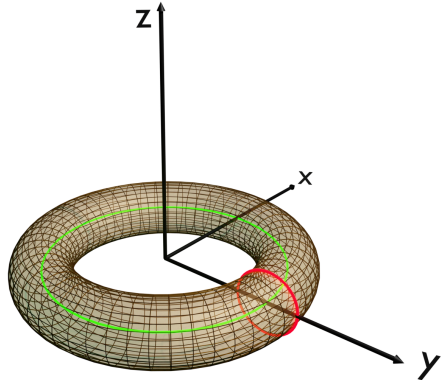


Figure 10: Diagram depicting a transparent wire loop modelled as a toroid positioned in the xy -plane with semi-major axis (green defined as A) and semi-minor axis (red defined as B).

The toroid was placed in the arbitrary xy -plane with the current density being set such that it models an AC current source:

$$\mathbf{J} = -J_0 \sin(\omega t) \cos(\varphi) \hat{x} - J_0 \sin(\omega t) \sin(\varphi) \hat{y} + 0 \hat{z} \quad (5.1)$$

where J_0 is the maximum current density, φ is the angle in the xy plane from the positive x -axis, and ωt is the angle measured from the positive z -axis, expressed in terms of the angular frequency ω and time t . It was chosen that the maximum current density was to be 1.0 Am^{-2} . The distribution of the current density is shown in figure 11 and is uniformly distributed in the z -direction.

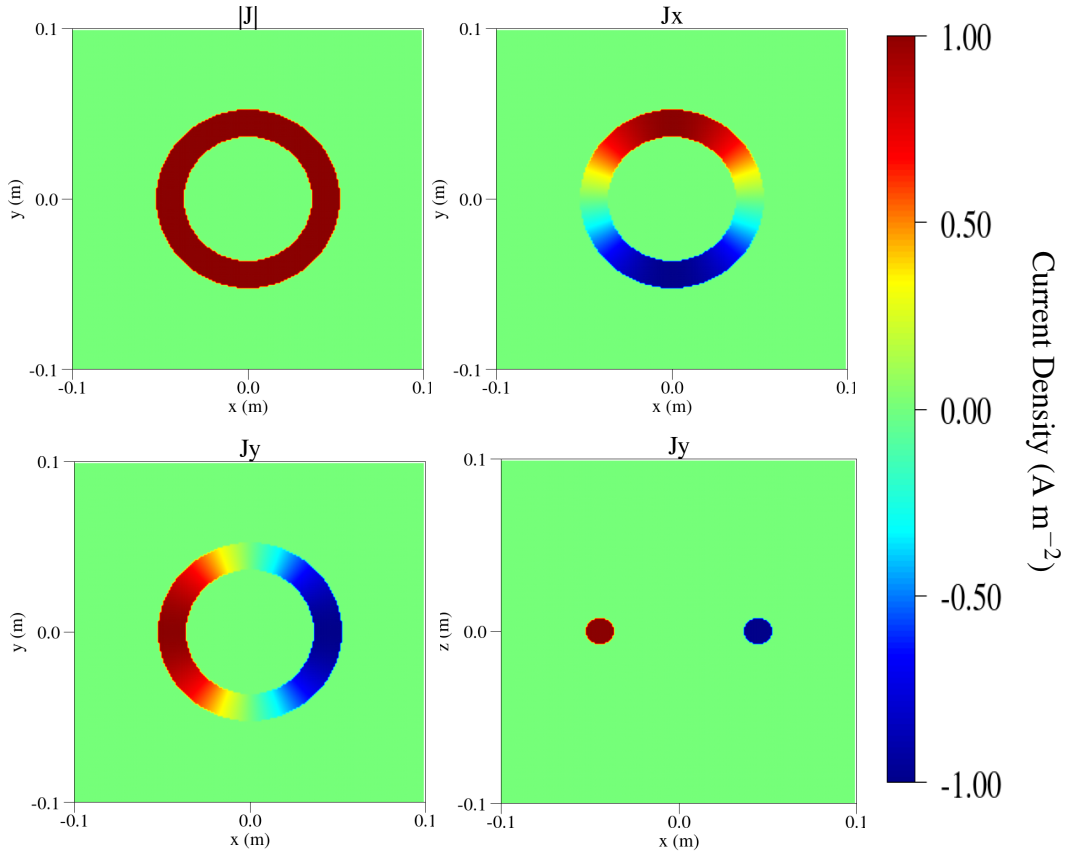


Figure 11: Colour plots highlighting the distribution of the current density within the wire loop at time step of 80. The current density is at a maximum. Simulation parameters: $w = 8.2 \times 10^{10} s^{-1}$, $\Delta x = 1mm$, $A = 45mm$, $B = 8mm$, $\Delta t = 4.8 \times 10^{-13} s$

5.2. Transparent Wire Loop Results

Originally, the significance of the choice of parameters was not understood, and so naively, the parameters were chosen only to satisfy the condition that multiple wave-fronts could be seen in the simulation. The current density was to reach its maximum in 80 time steps which gave a wavelength of 4.6mm, while the major radius of the toroid was set to 20mm. Figure 12 shows the preliminary result which is a reproduction of a previous student's results. As you can see, the propagation pattern does not match that of an infinitesimal dipole. The pattern of an infinitesimal dipole is that of a modulated sine curve with the principal lobe (region of max intensity) in the plane perpendicular to the dipole axis. The results obtained showed that the region of maximum intensity was in the side lobes and so the simulation was not that of a infinitesimal dipole. When excitation waves have a small wavelength, they are closely spaced. This can lead to destructive interference between scattered and incident

waves which could explain why the principal lobes become shifted to the side lobes. It could also be that the rapid phase shifts are causing near field effects to become more dominant.

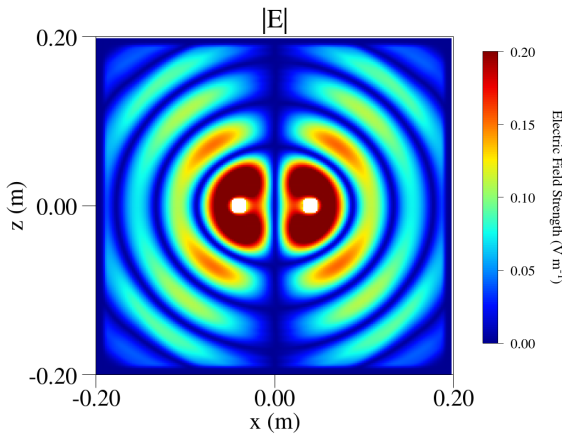


Figure 12: XZ-slice of a three-dimensional FDTD simulation of a wire loop (white) in the xy-plane with AC current flow. It captures the behaviour of the electric field when the excitation wavelength is smaller than the loop's circumference. Simulation parameters: source $\lambda = 4.6\text{ mm}$, $A = 20\text{ mm}$, $B = 4\text{ mm}$, $\Delta x = 1\text{ mm}$, $\Delta t = 4.8 \times 10^{-13}$, $t = 790$

In order to accurately model an infinitesimal dipole, the wavelength of the excitation source must be greater than the size of the toroid in the direction of the dipole moment (major radius). Therefore, for further results, a chose of angular frequency was such that the wavelength of the excitation source was now 4 times larger than that of the toroid loop. The toroid was then made smaller to 10mm in order for far-field propagation to be observed while still maintaining a small grid size of 200x200. Figure 13 demonstrates the improved results using the new parameters, which now match the analytic solutions for the infinitesimal dipole since the main lobes are now in the axis of the dipole moment of the wire loop. The arrows show the direction of the current which appear to be tangential to the wire loop as we hope.

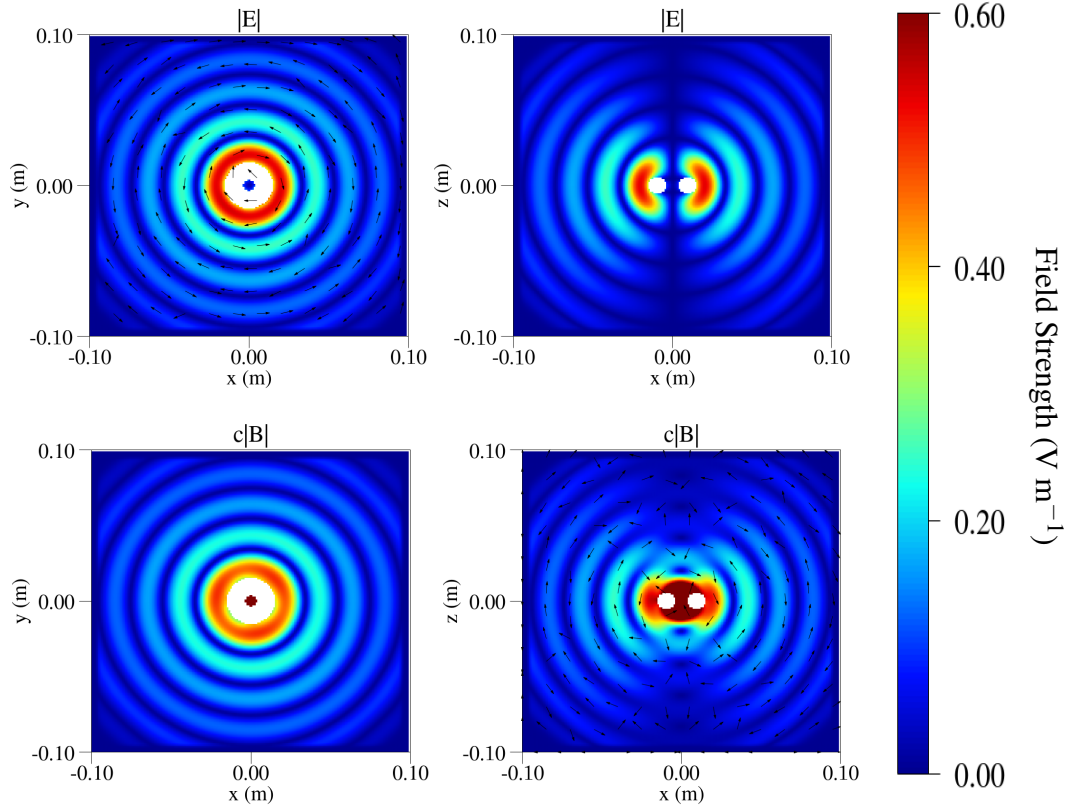


Figure 13: Still image three-dimensional FDTD simulation of a wire loop (white) in the xy-plane with AC current flow. The magnetic field has been scaled by the speed of light so that it matches the electric field magnitude. Simulation parameters: source $\lambda = 40\text{ mm}$, $A = 10\text{ mm}$, $B = 5\text{ mm}$, $\Delta x = 1\text{ mm}$, $\Delta t = 4.8 \times 10^{-13}\text{ s}$, $t = 790$

5.3. Conductive Wire Loop Results

The update equations with conductivity were tested for a value of $\sigma = 0$, which showed agreement with the non-conductive equations used for the transparent wire. Subsequently the conductivity was set to a high value which resulted in significant loss and minimal propagation. Obtaining predictive results at the extrema of conductivity gave confidence for further analysis.

A better model to that of a transparent wire would be that one considers the charge distribution to be maximum on a conductors surface, with exponential attenuation further into the material. The skin depth, δ , defines the distance where the current density becomes $1/e$ of its value at the surface [2]:

$$\delta = \sqrt{\frac{2}{\sigma \omega \mu}} \quad (5.2)$$

Where ω is the AC frequency, σ is the conductivity and μ is the magnetic permeability of the material. In a real system, the AC current positions itself due to the introduction of an AC voltage. It was decided that modelling the movement of the current density from a battery was unnecessary, as the primary interest lies in the solutions when the current has moved within the skin depth. Therefore, the current density was hard coded in a similar fashion to the transparent wire loop, while now being confined only within the skin depth. To model a realistic wire, a skin depth on the millimeter scale was required. One such material was a conductive polymer such as PEDOT:PSS ($\sigma = 1.0 \times 10^3 \text{ S/m}$) [12], which gave a skin depth of 4.04mm. Figure 14 shows the distribution of the current density now contained within the skin depth. Simulation of the conductive wire loop exhibited insufficient propagation due to the value of the conductivity being too large. Consequently, it was then decided that the conductivity only be placed in a tube radius of 2mm from the centre (away from the skin depth), so that the source was allowed to propagate at least once before attenuation. Therefore, each point in the transparent wire loop now contained x,y and z components matching that of the polymer.

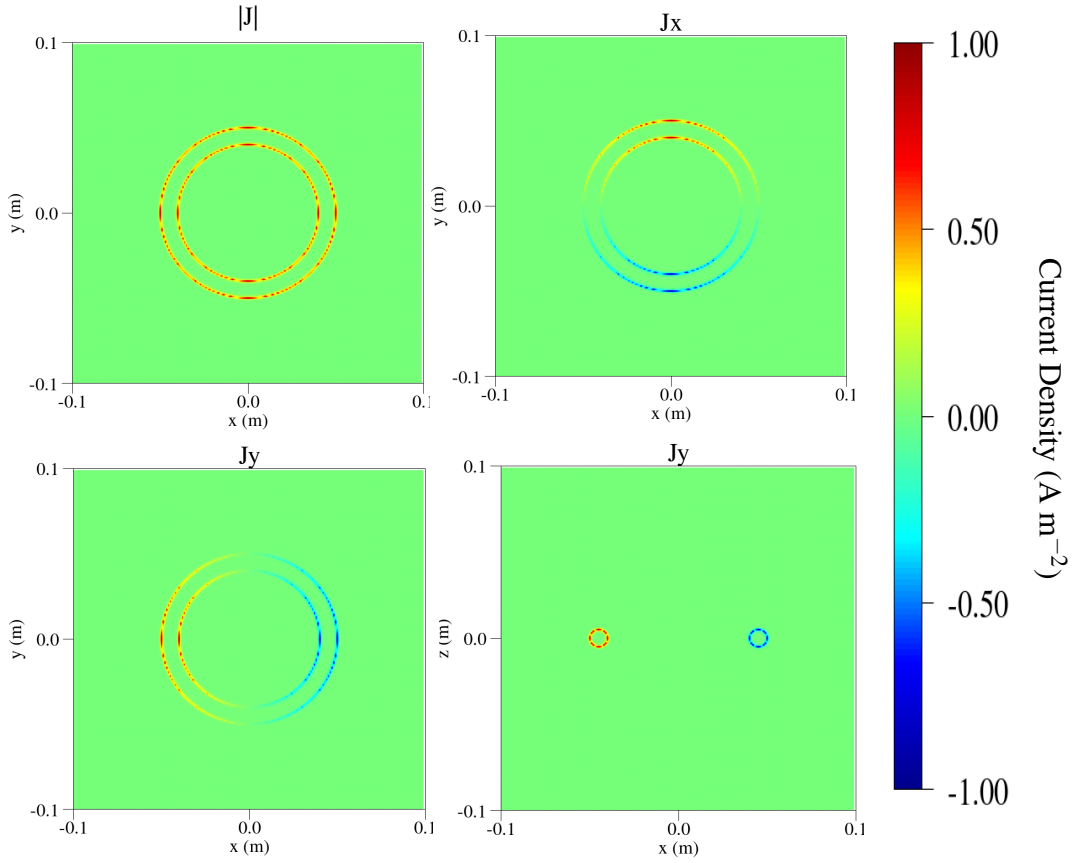


Figure 14: Colour plots highlighting the distribution of the value of the current density at a maximum. The current density is distributed within a wire loop according to the skin depth. Simulation parameters: source $\lambda = 40\text{mm}$, $\Delta x = 1\text{mm}$, $A = 45\text{mm}$, $B = 25\text{mm}$, $\Delta t = 4.8 \times 10^{-13}\text{s}$, $\delta = 4.04\text{mm}$

Figure 15 shows the results of a wire loop with the current density placed within the skin depth and the wire inner with a high conductivity. Our pattern mimics that of a transparent loop. We would expect that diffraction would increase the magnitude on the principal lobe and that diffraction would increase the magnitude on the side lobes. Our pattern mimics that of a transparent wire and so we may make the suggestion that these two affects balance out. However, our results must be taken with a pinch of salt as the solutions shown are asymmetric which could suggest the implementation of the conductivity was done incorrectly. Unfortunately due to the time constraints on the project this could not be investigated further.

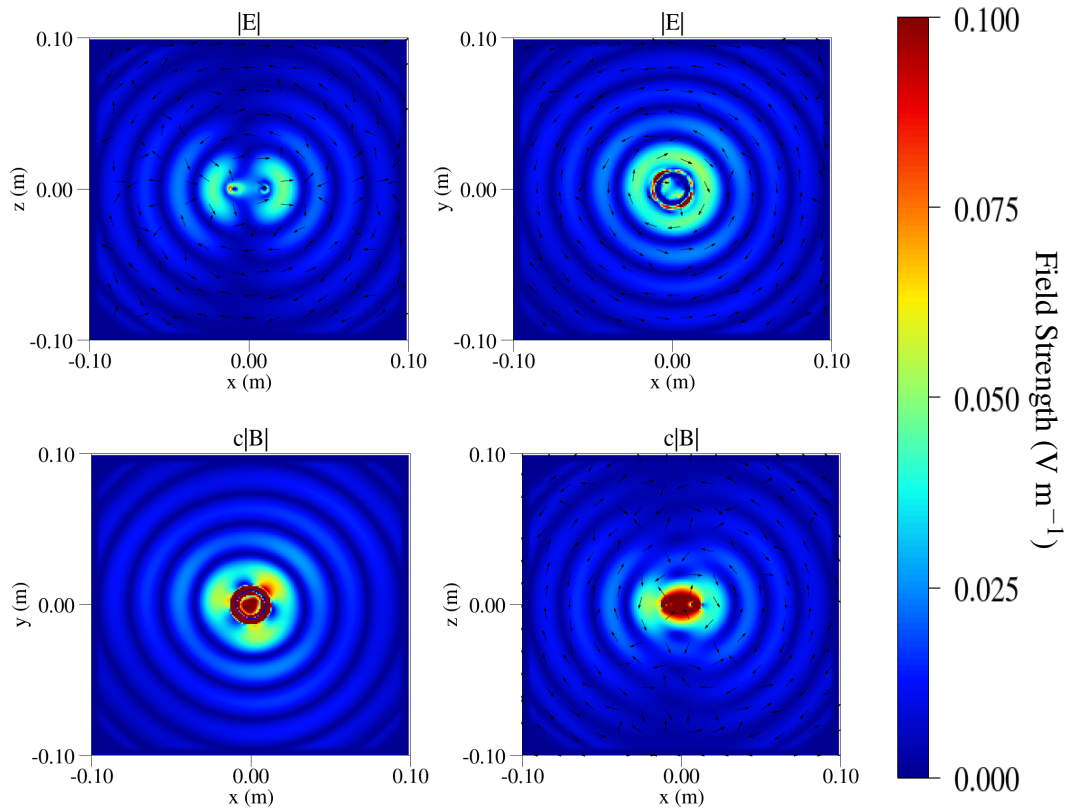


Figure 15: A still image from an FDTD animation of AC current in a wire loop. The current is contained within the skin depth and the wavelength of the source is made larger than that of the wire loop. The inner region of the wire loop tubes are highly conductive leading to exponential attenuation and partial reflections of waves that enter this area. Simulation parameters: AC $\lambda = 40\text{mm}$, $\Delta x = 1\text{mm}$, $A = 10\text{mm}$, $B = 5\text{mm}$, $\Delta t = 4.8 \times 10^{-13}\text{s}$

6. Discussion

6.1. Choosing FDTD

One of the primary reasons for choosing the FDTD method over other schemes was its simplicity and the wealth of knowledge available on the topic, making it easy to understand and implement. Despite there being many commercial software available, it was invaluable to build the software from the ground up. Studying previous work gave a good understanding, but it was only through hands-on experience that revealed the importance of conditions such as the CFL (courant-friedrichs-lewy). Many commercial software may not be optimised opting for consumer usability which is another benefit of self-making the software. Being able to easily customise the self-made software for a specific task enhances the utility.

6.2. Code Development

In achieving a high accuracy of the PML, its construction required creating a dual-grid system so that it could be customised for both the electric and magnetic fields, requiring twice the number of data points as the yee-grid. Hence, the limiting factor in this computation was the available RAM. The computation time was not the limiting factor and so the time step was chosen to be higher.

The software was initially developed in python and the graphs were plotted with the Matplotlib library, however, upon executing the 3D solutions, development halted and it became harder to debug due to the extended waiting time. It was then decided that it would be quicker to learn and implement the program in C than to wait for the python version. Once developed in C, solutions could be gained in real time, which sped up development considerably. Rather than shifting entire arrays through functions (computationally intense), in C the ability to use pointers as memory addresses saved computation time by orders of magnitude due to efficient data handling. C programs offers control over memory allocation and de-allocation which has which allows memory usage to be optimised. Having to explicitly declare variables allows the compiler to optimise the code based on known data types. The disadvantages to converting everything to C was the loss of Matplotlib library and the need to learn an alternative plotting software, GNUPLOT. The graphs for GNUPLOT were often too customisable with conflicting commands, and so creating the large commands needed to plot graphs from within the GNUPLOT terminal was time intensive. For future development, programming in C and feeding the data to a python build graph plotting tool would have been more efficient.

6.3. Future Improvements

To further enhance the speed of the FDTD algorithm, parallelisation techniques could be explored, including GPU processing, multi-core processing or a combination of both. It is hoped that future student can build on these solutions and explore conductivity in more depth.

7. Conclusion

In this project, an FDTD algorithm has been developed from first principles and, utilising the C programming language and with the absence of the supercomputer, was used to generate real-time three-dimensional solutions. The algorithm has demonstrated that it is a versatile and robust technique with the capability of handling many three-dimensional scenarios.

The update equations were upgraded via a modular process with validation techniques at each stage, with attempts also made to increase its accuracy. Once a verified algorithm was obtained, a wire loop was modelled and by carefully selecting parameters, was able to recreate the analytic solution of the Hertzian dipole. This then gave sufficient confidence to move forward onto more complex and realistic systems. An attempt was made to include conductivity, however, due to time constraints on the project, the results were deemed inconclusive.

8. Acknowledgements

The author would like to acknowledge Professor Hampshire for his continual support and input. The author would also like to acknowledge previous students Will Watson and Matthew Hooper for their work on the topic and well written reports.

9. References

- [1] K. S. Yee. *Numerical solution of the initial boundary value problems involving Maxwell's equations in isotropic media*. IEEE Trans, Microwave Theory and Techniques, vol. 44, pp. 61–69, 1998. DOI:10.1109/TAP.1966.1138693.
- [2] D. J. Griffiths. *introduction to electrodynamics; 4th ed.Re-published by Cambridge*. University Press in 2017. Boston, MA: Pearson, 2013. DOI:1108420419.
- [3] M. J. Hooper. *A New Approach to Current and Charge Distributions in Computational Electrodynamics*. 2016.
- [4] M. W. Watson. *Implementing a Numerical Method to Visualise the Electromagnetic Fields of a Magnetic Dipole and Wire Loop*, 2021.
- [5] D. B. Davidson. *Computational Electromagnetics for RF and Microwave Engineering*. Cambridge University Press, 2005. DOI:10.1017/CBO9780511611575.
- [6] R. Courant, K. Friedrichs, and H. Lewy *On the Partial Difference Equations of Mathematical Physic*. IBM Journal of Research and Development 11.2, (1967),pp. 215–234. DOI:10.1017/CBO9780511611575.
- [7] Kosuke Suzuki and Tatsuya Kashiwa *Reducing the Numerical Dispersion in the FDTD Analysis byModifying the Speed of Light*. Kitami Institute of Technology, Kitami, 090-8507 Japan. 2000.
- [8] EM Possible Figures provided by: .Lecture 13 (FDTD) – The Perfectly Matched Layer Youtube 2014.
- [9] Courant, R., Friedrichs, K., Lewy, H. *On the partial difference equations of mathematical physics*. IBM Journal of Research and Development, 11(2), 215-234. 1967.
- [10] Durham University - Professor Hampshire *Physics 2A lecture notes* 2021.
- [11] Young, H. D., Freedman, R. A. *Wave Optics. In University Physics with Modern Physics (15th ed., pp. 1187-1243)*. Pearson. 2019.
- [12] Thomas Stöcker, Anna Köhler, Ralf Moos *Why does the electrical conductivity in PE-DOT:PSS decrease with PSS content? A study combining thermoelectric measurements with impedance spectroscopy* 2012.

10. Appendix

10.1. Three Dimensional Update Equations

The three-dimensional FDTD update equations in a vacuum for non-magnetic materials using indices i , j , k , and time index t . We include a current density term along with an associated conductivity. Equations (7)-(9) included a complicated multiplicative term for the PML which is only active in the PML zones.

$$C_E^x|_{i,j,k} = \frac{E_{zi,j+1,k}^t - E_{zi,j,k}^t}{\Delta y} - \frac{E_{yi,j,k+1}^t - E_{yi,j,k}^t}{\Delta z}, \quad (1)$$

$$C_E^y|_{i,j,k} = \frac{E_{xi,j,k+1}^t - E_{xi,j,k}^t}{\Delta z} - \frac{E_{zi+1,j,k}^t - E_{zi,j,k}^t}{\Delta x}, \quad (2)$$

$$C_E^z|_{i,j,k} = \frac{E_{yi+1,j,k}^t - E_{yi,j,k}^t}{\Delta x} - \frac{E_{xi+1,j,k}^t - E_{xi,j,k}^t}{\Delta y}, \quad (3)$$

$$C_B^x|_{i,j,k} = \frac{B_z^{t+1/2}|_{i,j,k} - B_z^{t+1/2}|_{i,j-1,k}}{\Delta y} - \frac{B_y^{t+1/2}|_{i,j,k} - B_y^{t+1/2}|_{i,j,k-1}}{\Delta z}, \quad (4)$$

$$C_B^y|_{i,j,k} = \frac{B_x^{t+1/2}|_{i,j,k} - B_x^{t+1/2}|_{i-1,j,k}}{\Delta z} - \frac{B_z^{t+1/2}|_{i,j,k} - B_z^{t+1/2}|_{i,j,k-1}}{\Delta x}, \quad (5)$$

$$C_B^z|_{i,j,k} = \frac{B_y^{t+1/2}|_{i,j,k} - B_y^{t+1/2}|_{i-1,j,k}}{\Delta x} - \frac{B_x^{t+1/2}|_{i,j,k} - B_x^{t+1/2}|_{i,j-1,k}}{\Delta y}, \quad (6)$$

$$B_x^{t+1/2}|_{i,j,k} = B_x^{t-1/2}|_{i,j,k} + \frac{\Delta t}{\mu_0} C_E^x|_{i,j,k}, \quad (7)$$

$$B_y^{t+1/2}|_{i,j,k} = B_y^{t-1/2}|_{i,j,k} + \frac{\Delta t}{\mu_0} C_E^y|_{i,j,k}, \quad (8)$$

$$B_z^{t+1/2}|_{i,j,k} = B_z^{t-1/2}|_{i,j,k} + \frac{\Delta t}{\mu_0} C_E^z|_{i,j,k}, \quad (9)$$

$$CEE = \frac{1 - \sigma \Delta t}{2\epsilon} / \frac{1 + \sigma \Delta t}{2\epsilon}, \quad (10)$$

$$CEH = \frac{\Delta t}{\epsilon} / \frac{1 + \sigma \Delta t}{2\epsilon}, \quad (11)$$

$$E_x^{t+1}|_{i,j,k} = CEE \cdot E_x^t|_{i,j,k} + CEH \cdot (C_B^x|_{i,j,k} - \frac{\Delta t}{\mu_0} J_x^{t+1/2}|_{i,j,k}), \quad (12)$$

$$E_y^{t+1}|_{i,j,k} = CEE \cdot E_y^t|_{i,j,k} + CEH \cdot (C_B^y|_{i,j,k} - \frac{\Delta t}{\mu_0} J_y^{t+1/2}|_{i,j,k}), \quad (13)$$

$$E_z^{t+1}|_{i,j,k} = CEE \cdot E_z^t|_{i,j,k} + CEH \cdot (C_B^z|_{i,j,k} - \frac{\Delta t}{\mu_0} J_z^{t+1/2}|_{i,j,k}), \quad (14)$$

where Δt , Δx , Δy , and Δz are the time and spatial steps, E_x , E_y , and E_z are the components of the electric field, B_x , B_y , and B_z are the components of the magnetic field, J_x , J_y , and J_z are the components of the current density, ϵ is the permittivity, and σ is the conductivity. C_E^x , C_E^y , C_E^z , C_B^x , C_B^y , and C_B^z are the curl coefficients used in the update equations. CEE and CEH are the coefficients related to the conductivity.